HEALTH AND MEDICINE

Electro-assembly of a dynamically adaptive molten fibril state for collagen

Miao Lei¹, Xue Qu^{1,4}*, Haoran Wan¹, Dawei Jin³, Shijia Wang¹, Zhiling Zhao², Meng Yin³, Gregory F. Payne², Changsheng Liu¹*

Collagen is a biological building block that is hierarchically assembled into diverse morphological structures that, in some cases, is dynamically adaptive in response to external cues and in other cases forms static terminal structures. Technically, there is limited capabilities to guide the emergence of collagen's hierarchical organization to recapitulate the richness of biological structure and function. Here, we report an electro-assembly pathway to create a dynamically adaptive intermediate molten fibril state for collagen. Structurally, this intermediate state is composed of partially aligned and reversibly associating fibrils with limited hierarchical structure. These molten fibrils can be reversibly reconfigured to offer dynamic properties such as stimuli-stiffening, stimuli-contracting, self-healing, and self-shaping. Also, molten fibrils can be guided to further assemble to recapitulate the characteristic hierarchical structural features of native collagen (e.g., aligned fibers with D-banding). We envision that the electro-assembly of collagen fibrils will provide previously unidentified opportunities for tailored collagen-based biomedical materials.

Copyright © 2022
The Authors, some rights reserved; exclusive licensee
American Association for the Advancement of Science. No claim to original U.S. Government Works. Distributed under a Creative
Commons Attribution
NonCommercial
License 4.0 (CC BY-NC).

INTRODUCTION

Structural proteins are important building blocks in biology. Often, they enlist a variety of molecular interaction mechanisms to cue their hierarchical assembly into the complex morphological structures that confer controlled functional properties (1, 2). A classic example is collagen where triple helix molecules are cued to organize over a hierarchy of length scales as illustrated in Fig. 1A. In some cases, these hierarchical assemblies are connected through reversible interaction mechanisms to allow for structural reconfigurations and adaptive functional properties (3–6). Examples include the dynamic cross-linking of collagen fibrils by sea cucumbers that allows them to reversibly tune their mechanics to evade predation (7-9), the dynamical reversible associations between collagen fibers and between fibers and cells that allow them to induce cell migration and self-organization to facilitate wound healing and remodeling (10-12), and the reversible associated collagen fibers in cephalopod's skin allow heterogeneous organization under the stretching of muscle fibers to provide a means of camouflage (13–15). In other cases, irreversible interactions are used to connect collagen assemblies to yield terminal structures that maintain homeostasis over time scales that can range from days to lifetimes. Examples of such terminal structures include the covalently cross-linked collagen microfibrils of the transparent cornea (16, 17), the collagen fibrils of the stiff bone and teeth (18, 19), and the collagen fibers/fiber bundles of elastic skin and tough tendons (20–22).

Collagen is also an important technical material with various potential applications in tissue engineering, regeneration medicine,

and implantable medical devices (23–26). For instance, collagen-based membranes have been used in periodontal and implant therapy in clinic to promote the growth of specific types of cells. Collagen implants can also help heal cornea by supporting epithelia cells to the wound site (17, 27). Collagen textiles have been shown to stimulate tenogenesis for tissue repair (28). Collagen conduits are also used to guide Schwann cell migration and axonal regeneration for nerve repair (29). Besides, collagen–nano-inorganic composite that formed by biomimetic mineralization has been commercialized for bone repair (18, 30). Collagen-based conductive composites have been fabricated as a flexible sensor for wearable smart devices (31, 32).

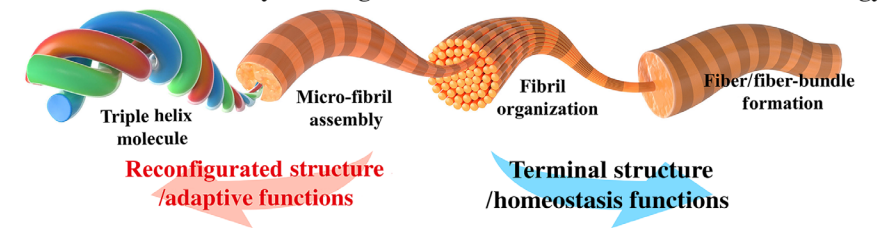
While it is easy to extract collagen triple helix molecules from biological tissues and to dissolve these molecular building blocks (33), it is generally not possible to control their bottom-up assembly over the various hierarchical length scales (23, 31, 34). Specifically, it is not yet possible to provide the spatiotemporally selective cues that can guide the formation of the intermolecular interactions responsible for the emergence of hierarchical structure. In the absence of fabrication methods that can recapitulate biology's ability to tune morphological structure and functional properties, it has been difficult to fully exploit the potential of collagen as a technological material.

Here, we report the electro-assembly of an intermediate molten fibril state for collagen that has partially aligned fibril structure but with limited further hierarchical organization. Figure 1B illustrates that this molten fibril state is generated in response to cathodic electrical input signals. The pH change resulting from the electrode reaction provides the cue that induces the positively charged collagen molecules from solution (pH 3.5) to assemble into fibrils at locations where the pH approaches its isoelectric point (Ip = 4.5). Furthermore, the applied electric field induces migration of the collagen molecules and also induces a partial alignment of the fibrils. Reversible physical interactions between the assembled fibrils results in the formation of a molten fibril network that is dynamically adaptive such that external cues can be applied to generate biomimetic dynamic multifunctions, such as stimuli-stiffening, stimuli-contracting, self-healing, and self-shaping. Moreover, this adaptive molten fibril

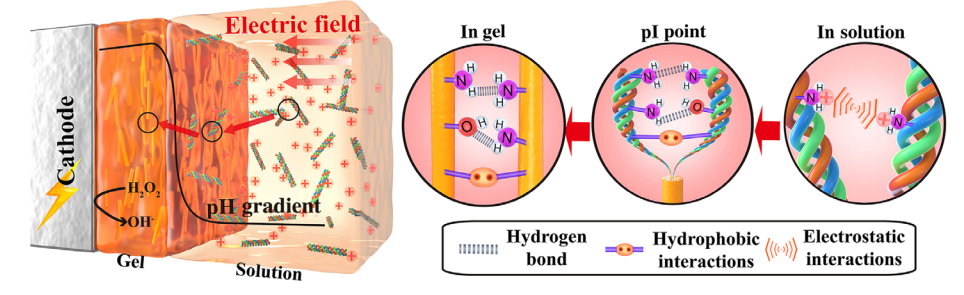
¹Key Laboratory for Ultrafine Materials of Ministry of Education, Frontiers Science Center for Materiobiology and Dynamic Chemistry, School of Materials Science and Engineering, East China University of Science and Technology, Shanghai 200237, China. ²Institute for Bioscience and Biotechnology Research and Robert E. Fischell Biomedical Device Institute, 5118 A. James Clark Hall, College Park, MD 20742, USA. ³Department of Cardiothoracic Surgery, Shanghai Children's Medical Center, School of Medicine, Shanghai Jiao Tong University, 1678 Dong Fang Road, Shanghai 200127, China. ⁴Shanghai Frontier Science Center of Optogenetic Techniques for Cell Metabolism, East China University of Science and Technology, Shanghai 200237, China.

^{*}Corresponding author. Email: quxue@ecust.edu.cn (X.Q.); liucs@ecust.edu.cn (C.L.)

A The hierarchical assembly of collagen and its diverse structure/functions in biology



B Electroassembly of molten fibril state for collagen



C Roadmap to recapitulate the biomimetic structures and functions for collagen

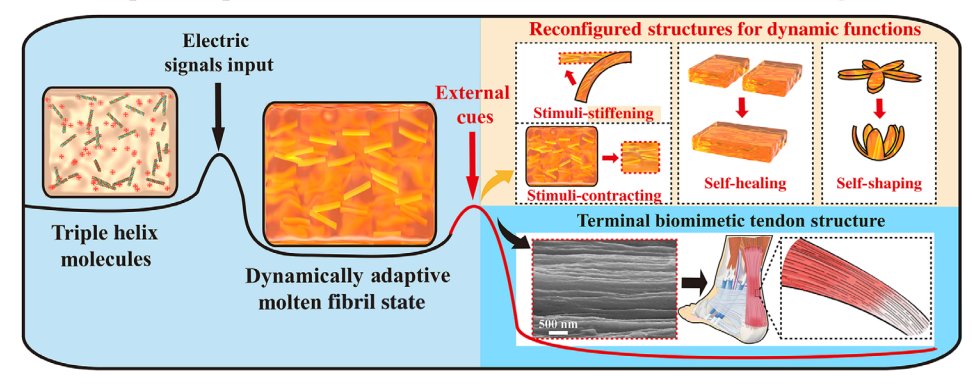


Fig. 1. Conceptual scheme of the dynamically adaptive molten fibril state for collagen based on the electro-assembly pathway. (A) Illustration of hierarchical assembly of collagen over length scales via diverse interaction mechanisms, reversible interactions of hierarchical assemblies allow for structural reconfigurations and adaptive functions, and irreversible interactions allow yielding terminal structures that maintain homeostasis in nature. (B) Illustration of the electro-assembly of collagen to create a molten fibril state and the mechanisms. (C) Roadmap that recapitulate the biomimetic structures and functions for collagen, electric signals input induce the dynamically adaptive intermediate assembly state formation, and selective external cues induce further functionalized assembly.

network allows reconfiguration of its hierarchical structure. Specifically, it enables further processing to produce terminal collagen matrices with stable higher-ordered hierarchical structure (i.e., aligned fibers with characteristic D-banding), to mimic the structures and mechanical properties of native collagen-based materials (e.g., tendon). Figure 1C summarized a roadmap to recapitulate the biomimetic structures and functions for collagen. We anticipate that the electro-assembly of an intermediate molten fibril state of collagen will provide previously unidentified opportunities to tailor collagen-based biomedical materials that better mimic and even recapitulate the structure and properties of native collagen materials.

RESULTS

Electro-assembly of collagen with molten fibril state

Acid-solubilized collagen I from porcine skin (designated as "Col") can form a transparent molecular solution in acetic acid solution (pH 3.5; Ip 4.5) (zeta potential and circular dichroism (CD) spectrum

in fig. S2 show right-handed triple helical collagen I). Such collagen solutions (0.5% w/v; pH 3.5; 0.1 M H₂O₂ added as sacrificial reductant for OH⁻ generation) can be induced to self-assemble onto a titanium foil by imposing a cathodic voltage when the solution pH is elevated to the collagen's Ip 4.5 (constant current 8 mA/cm², 15 min, 25°C; Fig. 2A and fig. S3). Figure 2B shows that electro-assembly yields a transparent collagen hydrogel film (designated as "EA-Col") of approximately 500 µm in thickness (80 µm after air drying). For comparison, collagen films of approximately the same thickness were prepared by a conventional solution assembly method (Fig. 2A and fig. S3), of which a shallow acidic solution of collagen (0.5% w/v; pH 3.5) was neutralized using sodium hydroxide to pH 7.2 and then casted and incubated at 37°C for 12 hours for film solidification (27, 35, 36). In contrast to electro-assembly, the solution assembly is a spontaneous process without external intervention. The images in Fig. 2C demonstrate that such cast collagen hydrogel films (designated as "SA-Col") have an opaque milky white appearance and, after air drying, remain semitransparent. The high transparency of EA-Col

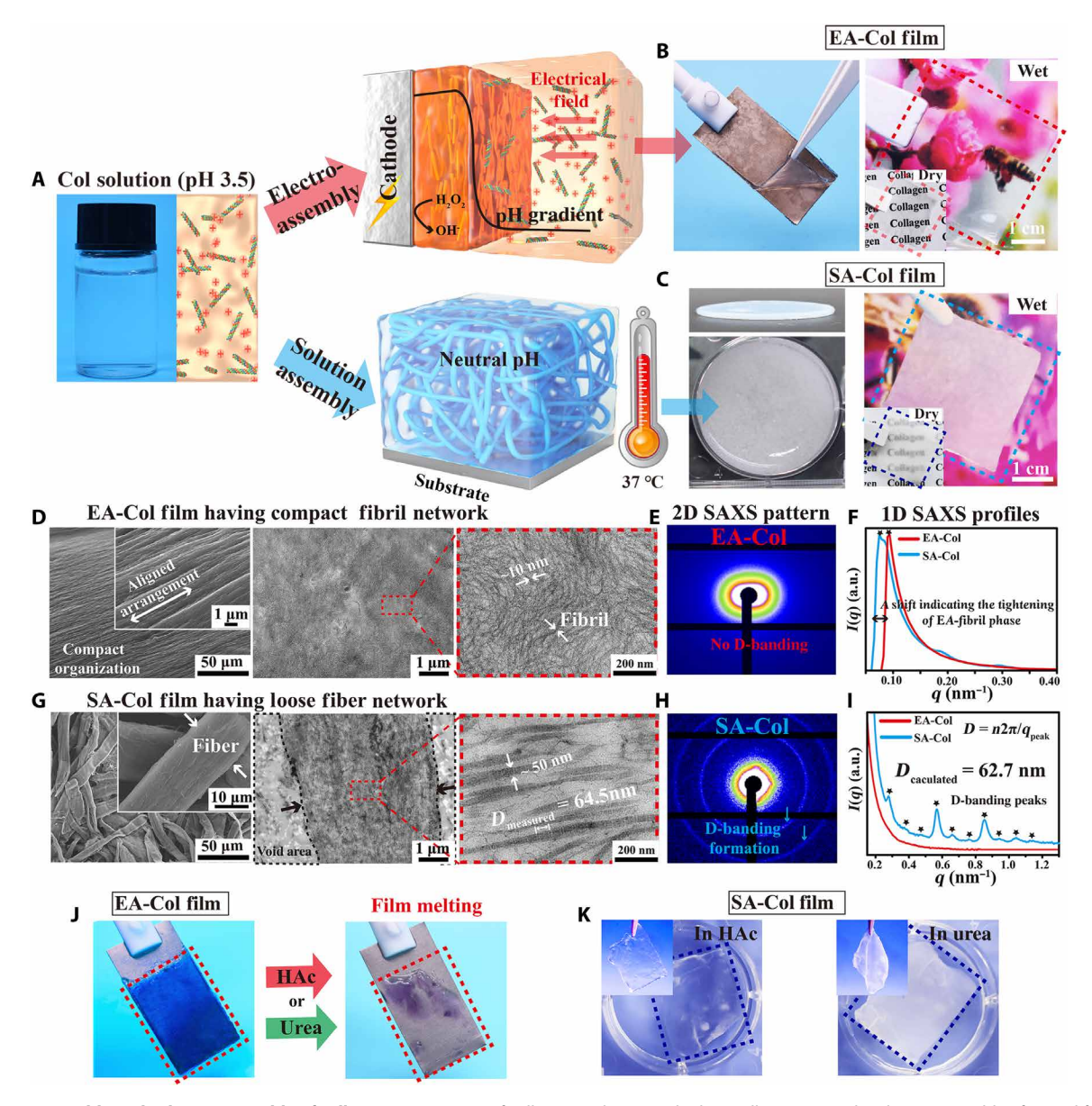


Fig. 2. Electro-assembly and solution assembly of collagen I. (**A**) Picture of collagen I solution and scheme illustrates (**B**) the electro-assembly of EA-Col film with superior transparency and (**C**) solution assembly of SA-Col film with opaque appearance. Photo credit: M.L., East China University of Science and Technology. Scanning electron microscopy/transmission electron microscopy (SEM/TEM) micrographs, synchrotron two-dimensional small-angle x-ray scattering (2D SAXS) scattering patterns, and 1D SAXS profiles of (**D** to **F**) EA-Col and (**G** to **I**) SA-Col. A shift toward higher *q* upon EA-Col in (**F**) indicates its tighter packing structure, and the EA-Col has no D-banding characteristics compared to SA-Col. The calculated D-banding space of 62.7 nm in (**I**) is close to the measured value of 64.5 nm in (**G**). a.u., arbitrary units. (**J**) EA-Col visualized by methylene blue rapidly dissolved in 0.1 M HAc or 0.1 M urea (a hydrogen bond interrupter), respectively, indicating the internal reversible interactions in EA-Col. (**K**) SA-Col is quite stable in above solutions and only swells a little bit when exposed in HAc solutions, indicating the existence of irreversible interactions in SA-Col. Photo credit: M.L., East China University of Science and Technology.

can be stabilized by chemical cross-linking (fig. S4), which may be beneficial for medical applications that require transparency over long time (e.g., corneal implants).

Microstructure analysis using scanning electron microscopy (SEM) and low magnification transmission electron microscopy (TEM) in Fig. 2D shows that the EA-Col film forms a densely organized structure (measured density $\approx 0.88~{\rm g~cm}^{-3}$) with aligned fibrous filamentous surface. High-magnification TEM further reveals that the EA-Col film is organized with fibrils in ~ 10 -nm diameter.

In contrast, Fig. 2G shows that the SA-Col film has a loose network ($\approx\!0.45~g~cm^{-3}$) with a random assembly of thicker fibers in $\sim\!10\mbox{-}\mu m$ diameter. The higher magnification TEM further suggests that the thicker fibers of the SA-Col film is composed of 50-nm-diameter fibrils with collagen's characteristic D periodic band (D-banding space $\approx 64.5~nm$), and more details about the structure are shown in fig. S5.

Nanostructure analysis was performed using the synchrotron small-angle x-ray scattering (SAXS; Fig. 2, E and H). Backgroundsubtracted SAXS profiles of the EA-Col film show a shift toward higher q (Q values range from 0.05 to 0.4 nm⁻¹, shown in Fig. 2F), which indicates tightening of the fibril phase packing. The two-dimensional (2D) SAXS pattern and respective 1D profiles (Q values range from 0.2 to 1.2 nm⁻¹, shown in Fig. 2I) show no evidence for D-banding formation in the EA-Col network, while the SA-Col network shows the characteristic scattering rings and 62.7-nm D-banding scattering peaks (as calculated by the Bragg equation).

It is worth noting that EA-Col and SA-Col are both intact in neutral but have completely different stability in acidic or urea media, as shown in Fig. 2 (J and K). EA-Col film dissolves quickly (<10 min) into the original electrolyte media, i.e., 0.1 M acetic acid aqueous at pH 3.5 or 0.1 M urea solution (a hydrogen bond interrupter), which indicates that the intermolecular associations of EA-Col film is mainly dependent on some weak interactions, for instance, H bond. In contrast, SA-Col that is produced by a prolonged thermal incubation is relatively stable in above solutions, only swells a little bit when exposing HAc. It may be because series of endothermic reactions are initiated during SA-Col formation, and thus, irreversible chemical bond, for instance, ketoimine bridges (23, 36), is established between the collagen molecules to give a stable internal network. More details on thermal stability are shown in fig. S6.

In summary, Fig. 2 demonstrates that the EA-Col network has a distinct partially aligned fibril structure but lacks the characteristic features of collagen's higher-order hierarchical structure as SA-Col (i.e., fiber and D-banding are absent). Presumably, the aligned fibril structure of this EA-Col emerges in response to the imposed electric field, while gel formation is induced by the localized high pH at the electrode surface. Moreover, unlike the static SA-Col network, the internal associations of EA-Col film are highly dynamic. Therefore, we use "molten fibril" to describe the dynamic and limited hierarchical collagen assembly in EA-Col, which is connected through reversible intermolecular interactions. While we use "static fiber" to describe the chemical bond bridged and higher-ordered collagen assembly in the SA-Col. The molten fibril state is an intermediate state that can be cued to "mature" into a higher-ordered terminal state with fiber formation and D-banding (as shown in fig. S7), it is presumably because the molten fibril state is energetically less favorable and can rearrange to assume D-banding under conducive conditions (37).

Dynamic adaptability of molten fibril to mechanical forces

Since the molten fibrils in E-Col are associated dynamically, we next evaluate their response to the mechanical forces. The images depicted in Fig. 3A show that the molten fibril-composed network is transparent and soft and undergoes substantial plastic deformation to adapt external mechanical forces upon stretching. It means that the reversibly connected fibrils can reconfigure their spatial network under the external forces. In contrast, the static collagen fiber-composed network shows an elastic response to mechanical force and restores its original structure. Representative stress-strain curves in Fig. 3B show that the molten fibril network is weak (i.e., low modulus), undergoes large deformation, and fractures gradually. In contrast, the static fiber network has a higher modulus, deforms to a small extent, and undergoes a brittle fracture. More details of the mechanical analysis are provided in the fig. S8.

To further investigate the dynamic adaptive process of molten fibrils to mechanical forces, we performed multicycle dynamic tensile loading measurements (0.2 N min⁻¹ for 10 cycles). The molten

fibril network was loaded between 0 and 0.04 MPa, and the results in Fig. 3C show comparatively large plastic deformation with notable hysteresis between loading and unloading cycles. In contrast, the static fiber network was loaded more than a larger range of stresses (0 and 0.16 MPa) yet shows comparatively small deformation (13.2% at 0.16 MPa) with tiny hysteresis between loading and unloading (Fig. 3D).

A somewhat unusual observation in Fig. 3C is the increase in Young's modulus (the slope of curve) that occurs with each consecutive loading cycle (summarized in Fig. 3E). This observed strain hardening is consistent with a stretching-induced reorganization of the molten fibril to a more orderly arrangement with strengthened fibril-fibril associations to resist deformation (the corresponding microstructural evidence is shown in Fig. 7). Consistent with this interpretation is the observation that this mechanical strengthening is accompanied by a decrease in the hysteresis between the loading and unloading cycles for each successive cycle. This change in hysteresis can be quantified by a deformation ratio (DR)

$$DR = \left(\frac{\varepsilon_y - \varepsilon_z}{\varepsilon_x - \varepsilon_z}\right) \times 100\% \tag{1}$$

where ε_x , ε_y , and ε_z are the strain after loading, the strain after unloading, and the strain before loading for each cycle. The plot in Fig. 3F shows that the molten fibril network has a large DR in the initial loading-unloading cycle, and this ratio progressively decreases approaching that of the static fiber network after the 10th cycle.

The last test to evaluate the differences in mechanical response is time-dependent stress relaxation measurement. To avoid the influence of the different strain ability of molten fibril network and static fiber network on this trial, we performed stress relaxation studies in two ways: either we produce a strain in the film by loading the same initial stress (0.1 MPa; 25°C; Fig. 3G) or we apply a stress to produce the same initial strain (20%; 25°C; fig. S8C, stress normalized to initial value). In both experiments, the molten fibril network undergoes greater stress relaxation, which implies that the reversibly connected fibrils could dissipate the external stress through the relative slip of molten fibrils. In contrast, the majority of the initially applied stress is stored in the static fiber network.

In summary, the results in Fig. 3 reveal a completely different mechanical response between the molten fibril and the static fiber networks. The dynamical associations in collagen fibrils allow them self-reorganize to adapt the mechanical cues much more flexibly when comparing to the covalently bonded static fibers.

Dynamic adaptability of molten fibril to Hofmeister ions

The mechanical variability of collagen tissue structure is particularly important for realizing important physiological functions. In nature, echinoderms like sea cucumbers can rapidly stiff their connective tissue to evade predation, which relies on the reversible regulation of the interactions among adjacent collagen fibrils (7, 8). Inspired by this, we use Hofmeister ions that are known to influence hydrophobic interactions to strengthen the internal connections of the collagen molten fibril network (38-40).

The sensitivity of the intermediate molten fibrils to Hofmeister series of ions is illustrated in fig. S9 (the Supplementary Materials show the effects of this salt series). The kosmotropic ions like ${\rm SO_4}^{2-}$ and ${\rm CO_3}^{2-}$ can stiff the molten fibrils network by strengthening the hydrophobic interactions among the film, while the chaotropic ions

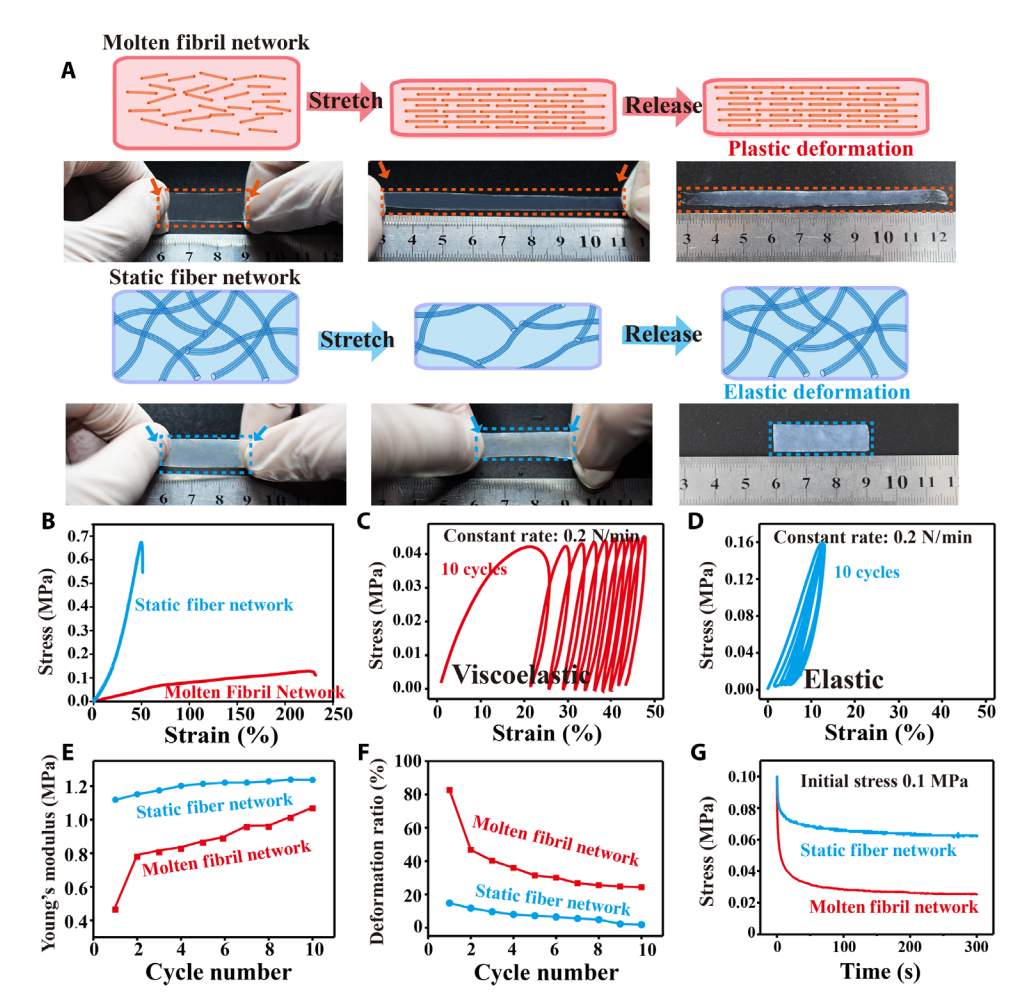


Fig. 3. The dynamic adaptability of molten fibril network to mechanical forces. (A) Visual evidence indicates that the molten fibril network (i.e., EA-Col) undergoes a plastic deformation, while static fiber network (i.e., SA-Col) shows an elastic deformation. Photo credit: M.L., East China University of Science and Technology. (B) The representative stress-strain curves and (C and D) cyclic loading-unloading curves show that the static fiber network undergoes little hysteresis between loading and unloading, while considerable hysteresis is observed with molten fibril network, which indicates that the static fiber network has elastic and molten fibril network has viscoelastic properties. (E) The increased Young's modulus and (F) the decreased shape deformation ratio of molten fibril network during the 10 cycles' loading and unloading indicate the internal structural reorganization ability of molten fibril network to adapt mechanical force. (G) The greater stress relaxation of molten fibril network further indicates that the process of mechanical adapting is accompanied with the dissipation of external stress. In contrast, the majority of the initially applied stress is stored in the static fiber network.

like I⁻ and SCN⁻ weakened the hydrophobic interactions, resulting in a swollen or even dissolved material.

We then compared the different mechanical response of molten fibril network and static fiber network to a strong kosmotropic salts [i.e., $(NH_4)_2SO_4$]. As depicted in Fig. 4A, the molten fibril network shows a biomimetic stimuli-stiffening behavior once exposed to $(NH_4)_2SO_4$ solution, which is due to the enhanced hydrophobic interactions. In contrast, the static fiber network in Fig. 4B is less responsive because the hierarchically organized fibers (versus molten fibrils) would have made full use of hydrophobic amino acid residues, as thus have a lower sensitivity to kosmotropic salts. Another possible reason is that the formation of covalent bonds restricts the free movement of collagen fibers.

A simple illustration in Fig. 4C shows that treatment of a molten fibril network with $(NH_4)_2SO_4$ (2 M for 24 hours) strengthens the network (the transparent film can withstand a 1-kg load) while retaining the network's flexibility (this film can be tied into a knot). In

contrast, treatment of the static fiber network with 2 M $(NH_4)_2SO_4$ had a small strengthening effect as the resulting film could not support a 500-g load (fig. S10).

To systematically evaluate the effect of the $(NH_4)_2SO_4$ on mechanical properties, we soaked molten fibril films and static fiber films in a series of $(NH_4)_2SO_4$ solutions (24 hours; room temperature) and then subjected these films to tensile testing. The stress-strain curves in Fig. 4D show that $(NH_4)_2SO_4$ treatment markedly strengthened the electro-assembled molten fibril films in a concentration-dependent manner. The same $(NH_4)_2SO_4$ treatment of the static fiber films showed much less marked strengthening. Figure 4E summarizes the effect on the Young's modulus: While both networks were strengthened by treatment with 4 M $(NH_4)_2SO_4$, the modulus for the molten fibril film increased 50-fold while that for the solution assembled static fiber film increased only sixfold. Figure 4F summarizes the effect on toughness: Treatment with 4 M $(NH_4)_2SO_4$ toughened the molten fibril film 16-fold but such treatment had

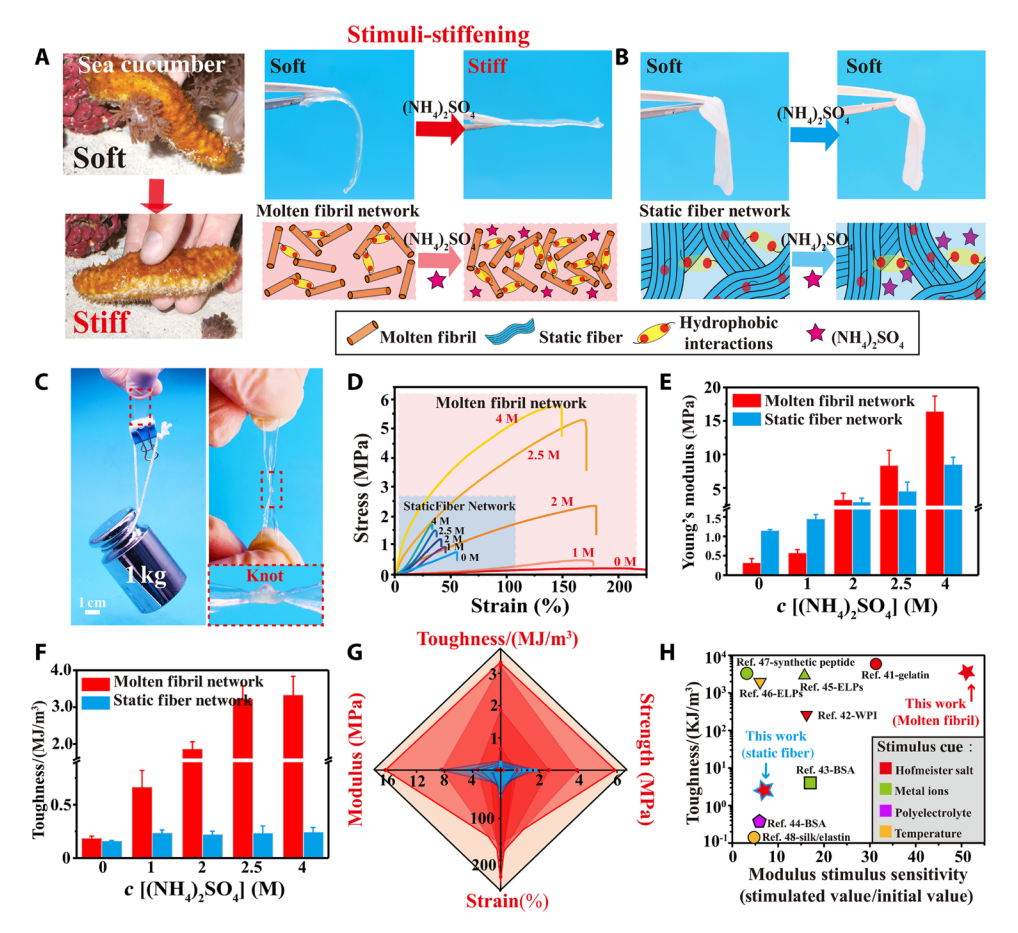


Fig. 4. The dynamic adaptability of molten fibril network to Hofmeister ions. (A) A nature model that sea cucumber can dynamically tune its mechanical properties between soft and stiff. The molten fibril network shows that a biomimetic stimuli-stiffening function triggered by a Hofmeister ion [e.g., $2 \text{ M} (\text{NH}_4)_2 \text{SO}_4$] enhanced fibril-fibril hydrophobic interactions. In contrast, (B) the static fiber network has no response to the same treatment, presumably due to the lack of available hydrophobic groups or the limited network reorganization. Photo credit: M.L., East China University of Science and Technology. (C) The pictures show the strong and tough mechanics of molten fibril network stimulated by (NH₄)₂SO₄. Photo credit: M.L., East China University of Science and Technology. (D) Stress-strain curves and (E and F) quantitative Young's modulus and toughness of molten fibril network and static fiber network treated by various concentrations of (NH₄)₂SO₄, indicating a much more substantial strengthening to the molten fibril network vs static fiber network. (G) A spider diagram quantitatively summarizes the effects of (NH₄)₂SO₄ on the mechanical properties of the collagen network, indicating that the molten fibril network (red area) has a much more mechanical flexibility compared to the static fiber network (blue area). (H) The modulus stimulus sensitivity (i.e., the ratio of the stimulated modulus to the initial modulus) comparison among molten fibril network, static fiber network, and other protein networks to external stimuli reported in references (e.g., Hofmeister salt, metal ions, and temperature). Picture of sea cucumber reproduced with permission (7). Copyright 2008 American Association for the Advancement of Science.

little effect on the static fiber film. Further analysis from dynamic loading and unloading measurements (figs. S11 and S12) shows that the high toughness of the molten fibril state is mainly due to its ability to dissipate a large fraction of energy through plastic deformation.

Figure 4G shows a spider diagram that quantitatively summarizes the effects of $(NH_4)_2SO_4$ on the mechanical properties of the molten fibril films. This plot shows that the molten fibril network (shown in the red area) is highly responsive to $(NH_4)_2SO_4$ compared to the static fiber network (shown in the blue area). A broader comparison (Fig. 4H) again shows the high modulus stimulus sensitivity of the molten fibril state network to $(NH_4)_2SO_4$ treatment is considerably larger than the modulus stimulus sensitivity of static fiber state network and other protein networks to external stimuli used to adjust noncovalent interaction mechanisms (e.g., Hofmeister salt, metal ions, and temperature). References summarized in table S3 and the Supplementary Materials (41–48). In summary, Fig. 3 illustrates that

collagen's adaptive molten fibril state is highly responsive to Hofmeister series of ions cues capable of adjusting physical cross-linking through hydrophobic interactions that allow widely and reversibly tailor of molten fibril network's mechanical properties.

Hofmeister ion-strengthened molten fibril network provides dynamic mechanical functions in vivo

Considering the strengthen process of molten fibril network by Hofmeister effect is reversible (i.e., the molten fibril network is strong when ions exist in network and the molten fiber network will return to a soft state when the ions leaching from the network), one biomedical application was considered to illustrate how the adjustable and emergent properties of the molten fibril network could be used to meet a design objective that changes mechanics over time. Figure 5A illustrates that, in some surgical interventions (e.g., traditional decompression pulmonary artery surgery), a band is implanted around an artery to constrict blood flow and protect a

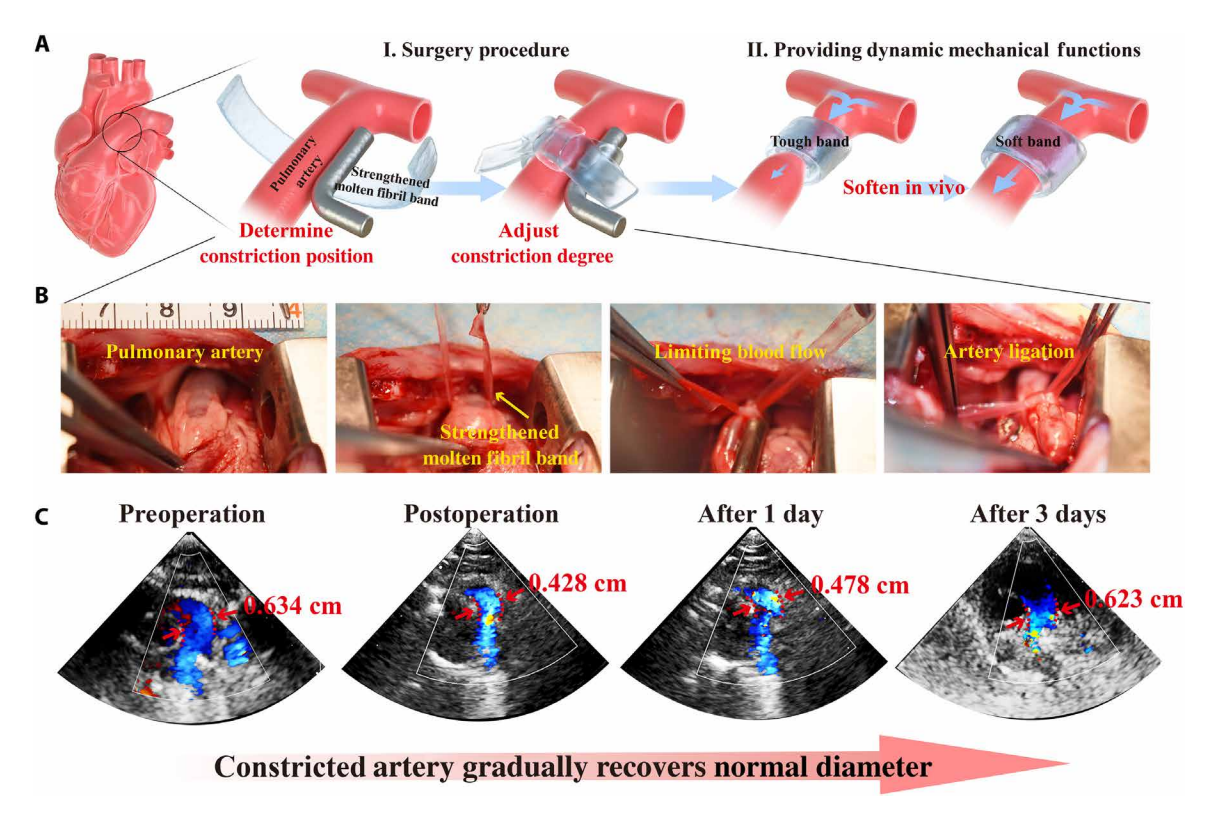


Fig. 5. The strengthened molten fibril network provides dynamic mechanical functions in Vivo. (A) The illustration of a strengthened molten fibril band providing an initial high strength with dynamic relaxation over time in vivo for a decompression pulmonary artery surgery. (B) Photograph of the surgery process using $2 \, M \, Na_2 CO_3$ strengthened molten fibril band. Photo credit: M.L., East China University of Science and Technology. (C) Color Doppler ultrasound observation of the diameter of pulmonary artery over time, indicating that strengthened molten fibril band can provide a short-period mechanical restraints and then soften after 3 days to recover the normal pulmonary artery diameter and blood supply.

vulnerable downstream site from hypertension. Immediately after surgery, this band should be strong to ensure significant constriction, but, over time (e.g., as the heart strengthens), the band should relax to allow greater blood flow (the timing varies depending on clinical details) (49-51). Thus, an ideal material for this band would have mechanical properties that dynamically relax under in vivo conditions. We envision that a molten fibril network that has been strengthened by a Hofmeister salt could be used for such applications as the initial high strength would be expected to relax as this salt leaches from the network.

For this biomedical demonstration, we used the biocompatible Na₂CO₃ salt (2 M) to strengthen a molten fibril film to serve as a banding material (the softening of strengthen film in vitro is described in fig. S13). Using New Zealand rabbits as our animal model, we applied a Na₂CO₃-strengthened molten fibril film as a band to decrease the diameter of pulmonary artery as illustrated in Fig. 5B. The cardiac color Doppler ultrasound images in Fig. 5C show that surgical banding reduced the diameter of the pulmonary artery by 68% from $\Phi = 0.63$ cm (preoperative) to $\Phi_0 = 0.43$ cm (postoperative), confirming that an implanted band prepared from a Na₂CO₃strengthened molten fibril film constricts the diameter of the pulmonary artery and restricts blood flow. The diameter of the pulmonary artery increased to 75% of normal diameter after the first day ($\Phi_1 = 0.48$ cm) and returned to its preoperative diameter after 3 days. This in vivo result is consistent with in vitro measurements (discussed in the Supplementary Materials) that show that

leaching of the Hofmeister salt from the molten fibril networks results in dynamically adjusting mechanically properties. Over a longer time, this strengthened molten fibril band is expected to be resorbed as illustrated by preliminary biodegradation studies with the enzyme collagenase (fig. S14).

Dynamic adaptability of molten fibril network to anionic clusters

Except for adjusting hydrophobic interactions in the molten fibril film, we also investigate the possibility to reconfigure the structure and properties of molten fibril network by regulating the electrostatic interactions. Introducing electrostatic interactions through metal anionic clusters is a common strategy (52–54). Here, gold ionic cluster ($n \times [\text{AuCl}_4]^{n-}$) is chosen as a model because of gold's excellent biocompatibility and its ability to confer advanced properties (e.g., high conductivity and photothermal transformation) (55, 56).

In our studies, we soaked the molten fibril and static fiber films in the solutions of chloroauric acid (HAuCl₄; 0.1 M; pH 2; room temperature). Figure 6 (A and B) shows that both films became yellow in color upon gold treatment, while the molten fibril network underwent considerable stimuli-contracting. Contraction of the molten fibril network is rapid and occurs over the course of 10 min, while no shrinkage was apparent for the static fiber network (Fig. 6C). Spectra from x-ray photoelectron spectroscopy (XPS) and x-ray diffraction (XRD) (Fig. 6, D and E) indicate that gold ionic clusters are present in both networks. Presumably, the marked

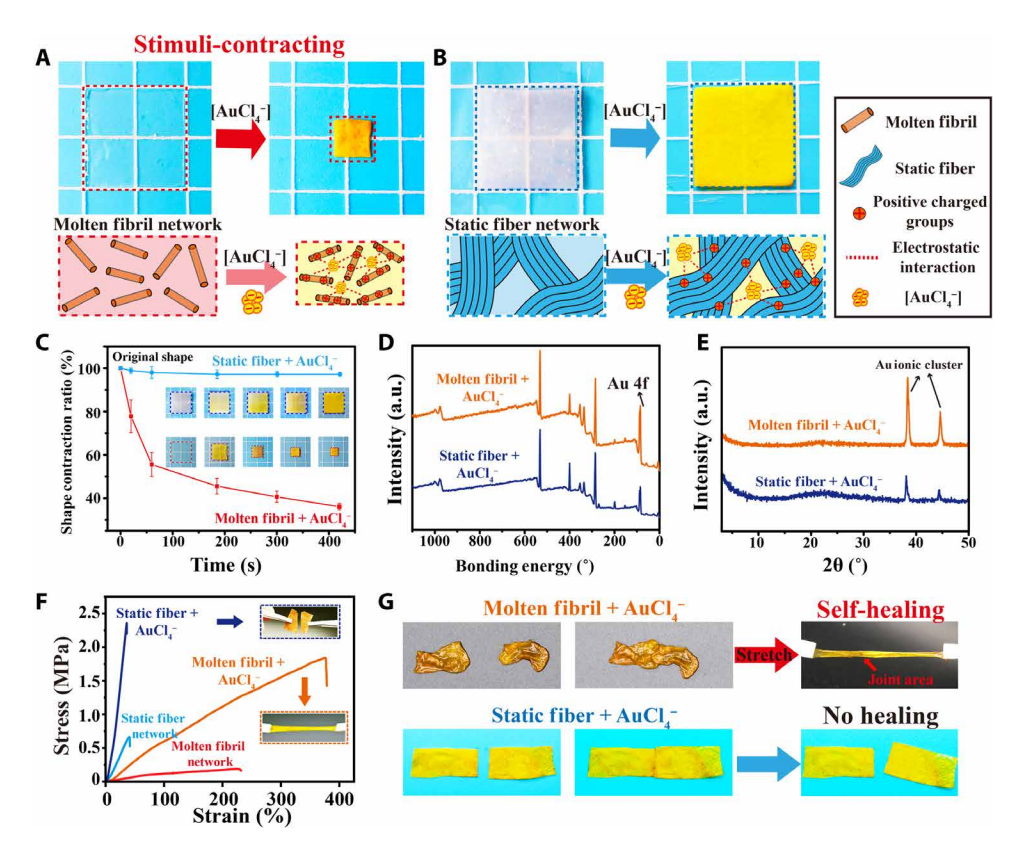


Fig. 6. Dynamic adaptability of molten fibril network to anionic clusters. (**A**) Visual evidence indicates the molten fibril network undergoes a considerable stimulicontracting by gold ionic clusters (i.e., $n \times \text{AuCl}_4^-$) induced electrostatic interactions. In contrast, the static fiber network in (**B**) shows no shape response after the same treatment, presumably because the strong cross-linking limits the reorganization of fibers in the network. Photo credit: M.L., East China University of Science and Technology. (**C**) The kinetics of shape contraction of the two networks after 0.1 M AuCl_4^- stimulating. (**D**) X-ray photoelectron spectroscopy (XPS) and (E) x-ray diffraction (XRD) further prove the presence of AuCl_4^- in the networks. (**F**) The stress-strain curves show that both networks are strengthened by 0.1 M AuCl_4^- treatment for 1 hour; however, the static fiber network remains brittle with low fracture strain, while the molten fibril network shows increased toughness and fracture strain. (**G**) The AuCl_4^- -treated molten fibril network shows self-healing properties consistent with a reversible electrostatic cross-linking mechanism. The static fiber network does not show such property, consistent with its strong cross-linking—limiting its ability to dynamically reconfigure. Photo credit: M.L., East China University of Science and Technology.

gold-induced shrinkage of the molten fibril network (but not static fiber network) occurs because the molten fibril's physical interaction allows for a greater dynamic reconfiguration of the network.

Gold treatment significantly alters the properties of both the molten fibril and static fiber networks. Mechanical testing shows that both networks are strengthened by gold treatment (Fig. 6F); however, the static fiber network remains brittle with low fracture strain, while the molten fibril network shows increased toughness and fracture strain. The gold-treated molten fibril network shows self-healing properties (Fig. 6G) consistent with a reversible electrostatic cross-linking mechanism. The static fiber network does not show such self-healing properties after gold treatment. Consistent with its covalent bond, bridged connection is limiting its ability to dynamically reconfigure. A continuous shear experiment provides more evidence for the self-healing properties of the gold-treated molten fibril network (see fig. S15).

Janus collagen film with molten fibril/static fiber networks provide programmable 3D self-shaping functions

Cephalopods create complex 3D papillae shapes (such as vertically flat or trilobed) by organizing the heterogeneous structure of the skin. The contractile erector layer bottom is used to control the 3D shape, and the stretchable elastic layer below is used to connect the

soft tissue in papillae (13, 15). Inspired by this, we used molten fibril network and static fiber network to synthesize a asymmetric collagen composite material (named "Janus collagen film") with similar heterogeneous structure, which was stimulated by metal ionic clusters (i.e., $n \times [\mathrm{AuCl_4}]^{n-}$) to achieve programmable 3D self-shaping. Figure 7A shows that we created bilayers composed of molten fibril layer as the stimuli-contracted layer and static fiber layer as a stretchable elastic layer. Experimentally, the prepared hydrated molten fibril film and static fiber film (the thickness of both is controlled at about 500 µm) are combined and dried together at room temperature. The two film networks adhered together to form a collagen-based Janus bilayer that remained firmly adhered after rehydration.

Initial stimulus that induced self-shaping of Janus collagen film was demonstrated by immersing the strip- shaped Janus collagen bilayer sample ($2.0 \times 0.5 \times 0.1$ cm) in 0.1 M [AuCl₄]⁻ at room temperature, as shown in Fig. 7B. The Janus collagen film generated a bending movement and gradually formed to completely closed ring 362° (Fig. 7B and movie S1). Despite this substantial deformation, the two films remained strongly adhered presumably due in part to the self-healing properties of the gold-treated molten fibril layer.

The shape of the Janus collagen film can be tailored arbitrarily to achieve different 2D shapes, such as a flower shape (as shown in

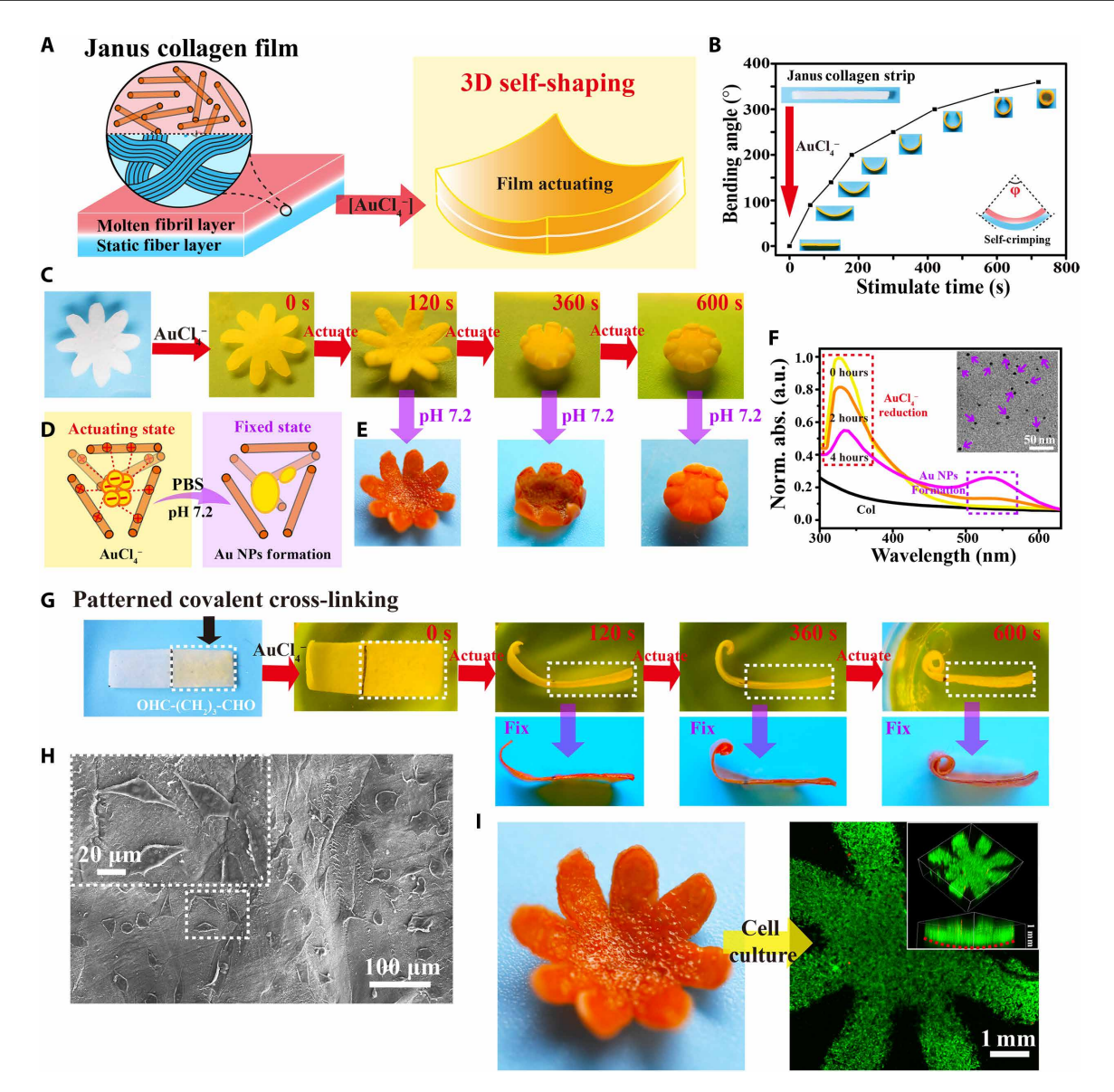


Fig. 7. The programmable 3D self-shaping function of Janus collagen film. (A) Illustration of integrating the molten fibril network and static fiber network into a Janus collagen film to realize self-shaping under external stimuli AuCl₄⁻. (B) Kinetic bending of Janus collagen strip by the stimuli of 0.1 M AuCl₄⁻. (C) 3D self-shaping process of a planar flower-shaped Janus collagen film in 0.1 M AuCl₄⁻. Photo credit: M.L., East China University of Science and Technology. (D) Mechanism of fixing temporary 3D shape by transferring the Janus collagen film into phosphate-buffered saline (PBS) (pH 7.2) that can induce the reduction of AuCl₄⁻ into gold nanoparticles (AuNPs) and eliminate the electrostatic cross-linking interactions. (E) Visual images of fixed intermediate 3D shapes. Photo credit: M.L., East China University of Science and Technology. (F) The ultraviolet–visible spectroscopy (UV-vis) spectra and TEM image further prove the reduction of AuCl₄⁻ to Au particles in the deformed Janus film after soaking in PBS. Norm. abs., Normalized absorbance. (G) 3D self-shaping process of a patterned covalently cross-linked Janus collagen film (white box indicates the area cross-linked by 0.1% glutaraldehyde) and the visual images of fixed intermediate 3D shapes. Photo credit: M.L., East China University of Science and Technology. (H) After PBS treatment, the generated Janus collagen–AuNP composite film supports the adhesion of L929 fibroblast for 24 hours. (I) The cells cultured on a Janus collagen–AuNP composite with a 3D petal structure for 21 days show a high activity, as indicated by a LIVE/DEAD cell staining.

Fig. 7C). After immersing the Janus collagen film into 0.1 M $[\mathrm{AuCl_4}]^-$ at room temperature, the 2D flower sheet can gradually transform into various 3D shapes over time (movie S2). The use of gold as the stimulus also allows intermediate temporary shapes to be fixed by transferring the Janus collagen film into a neutral buffer system [phosphate-buffered saline (PBS) (pH 7.2)] that can induce the reduction of $\mathrm{AuCl_4}^-$ into gold nanoparticles (AuNPs). Such reductions have been reported to occur spontaneously through the oxidation of collagen's hydroxyproline residues (57), and this

conversion is expected to eliminate the electrostatic cross-linking interactions between the $n[\mathrm{AuCl_4}]^{n-}$ and positively charged collagen chains as illustrated in Fig. 7D. Visual evidence for this conversion is the observed color change in Fig. 7E from light yellow ($\mathrm{AuCl_4}^-$) to orange (AuNP), while spectrophotometric evidence for this reduction is the change in absorbance from 330 to 540 nm (AuNP formation) (Fig. 7F). TEM images at the right confirm the presence of well-defined AuNPs with a diameter range of 5 to 10 nm (marked with arrows).

The complexity of the shape deformations of the Janus collagen film can be further modulated by introducing covalent cross-links that confer rigidity into some regions of the bilayer film. Experimentally, we introduced covalent cross-links by partially dipping our Janus collagen film into a solution of the chemical cross-linking reagent (e.g., 0.1% glutaraldehyde) as indicated by the white boxed area in Fig. 7G. After immersing this patterned cross-linked Janus collagen film in 0.1 M [AuCl₄] $^-$ solution, the uncross-linked Janus region deforms as expected; the covalently cross-linked region does not deform; and the deformed shape can be "fixed" at any time by transferring to film into a neutral buffer system (PBS, pH 7.2) at room temperature to induce the reduction of [AuCl₄] to AuNPs (movie S3 shows this shape deformation, while fig. S16 shows additional evidence for the transformation and fixing of various 3D Janus collagen film shapes at room temperature).

We anticipate that, after PBS treatment, the generated Janus collagen–AuNP composite film has good biocompatibility, and an initial biocompatibility test for the Janus collagen–AuNP composite film was performed using L929 fibroblast cells. These cells were observed to adhere and spread on these composite films, as shown in the SEM images of Fig. 7H. And the LIVE/DEAD cell staining and CCK-8 results further proved the proliferation of cells on these composite films (fig. S16). This allows that, to culture cells on a Janus collagen–AuNP composite film with a specific 3D structure, as shown in Fig. 7I, L929 fibroblasts could be cultured on a specific 3D petal structure for a long time (21 days) with a high survival rate.

In summary, the molten fibril network also can be induced to dynamically reorganize in response to metal anionic clusters (e.g., gold cluster), and transforming from a weakly associated state to a strong electrostatic complexation state, this transformation confers stimuli-contracting and self-healing properties. In particular, a previously unknown chemical-actuating strategy was proposed to realize programmable self-shaping from 2D to 3D of Janus collagen film and construction of specific 3D structure metal-protein platforms with good biocompatibility, which presumably could be promising candidates for application as bioactuators, soft robots, and other intelligent biomimetic devices.

Aligned stable fibril network processed from molten fibril network

The above results indicate that collagen electro-assembly can yield an intermediate molten fibril state with limited hierarchical organization but with a partially aligned collagen nanostructure that is connected through responsive physical interactions. This allows the molten fibril network to be reconfigured to adapt external cues (i.e., mechanical force, Hofmeister ions, and metal ionic clusters) and generate biomimetic dynamic multifunctions, such as stimulistiffening, stimuli-contracting, self-healing, and self-shaping. Another potential advantage of the molten fibril state is that processing may allow the molten fibril network to be further aligned by straining, after which this aligned fibrils can be permanently fixed by covalent cross-linking to form aligned stable fibril structures (named "ASF structures") as suggested in Fig. 8A.

Experimentally, molten fibril films (0.5-mm thickness) were prepared and mechanically stretched to different strains, after which these films were fixed using ultraviolet (UV)/riboflavin cross-linking (experimental details in the Supplementary Materials). For comparison, a control cast static fiber film was prepared and cross-linked by UV/riboflavin cross-linking. Structural evidence for

the strain-induced alignment of the molten fibril network was provided by three independent methods.

First, the images from polarizing optical microscopy (Fig. 8B) show that no obvious optical birefringence was observed for the control static fiber network, indicating an isotropic structure; some optical birefringence was observed for the unstrained molten fibril network, indicating partial alignment; and more intense optical birefringence was observed for films that had been strained to greater extents, indicating a strain-induced alignment of the fibrils. Second, the TEM cross-sectional images (Fig. 8C) indicate that the control static fiber network has a loose and isotropic structure (the red circles indicate fibers that are aligned perpendicular to the cross section), while the strained molten fibril films have nanostructures that are denser and more aligned. Last, the 2D SAXS patterns (Fig. 8D) for the control static fiber network shows a ring of nearly uniform intensity consistent with an isotropic structure, while the elongated longitudinal pattern for the strained molten fibril films is consistent with an anisotropic aligned nanofibril structure. A quantitative description of the orientation degrees is the Herman's orientation parameter (f_c) , which can be determined from the azimuthal-integrated intensity distribution curves of the x-ray scattering patterns. For an isotropic material, $f_c = 0$, and for an ideal uniaxially oriented material, $f_c = 1$. Fig. 8D shows the control static fiber network had little alignment ($f_c = 0.02$), while the molten fibril network showed alignment that increased from $f_c = 0.15$ for the unstrained network to $f_c = 0.93$ for the network that had been strained 200%. These results indicate that strain of the molten fiber network induced long-range alignment of the molten fibril architecture along the direction of strain. Further analysis of these SAXS results in Fig. 8E shows the azimuthal-integrated intensity distribution curves that gradually narrowed with the increasing strain for molten fibril network.

Strain-induced alignment of the molten fibril structure is expected to confer anisotropic mechanical properties to the films. To test this expectation, we prepared molten fibril films with varying strain degree, fixed these films by UV/riboflavin cross-linking, and then measured the mechanical properties of the wet films. Figure S17 shows that UV-induced cross-linking of the unstrained molten fibril network (0% ASF) markedly changed its mechanical properties, making it stronger, more elastic, and brittle compared to the uncross-linked molten fibril film. When the molten fibril films were cross-linked after strain-induced alignment, the generated ASF films show a marked enhancement in the mechanical properties when they were tested parallel to the direction of alignment (i.e., a 10-fold increase in modulus). In Fig. 8F, when these ASF films were tested perpendicular to the direction of fibril alignment, the modulus was substantially reduced. Figure 8G summarizes the anisotropic mechanical properties of these wet molten fibril films after their strain-induced alignment and subsequent cross-linking.

Biomimetic preparation of a terminal tissue "tendon" with aligned hierarchical fiber structure

While mechanical stretching of the electro-assembled molten fibril collagen network could generate a highly aligned and densified fibril structure, this network still lacks the higher-order hierarchical features (i.e., fibers and D-banding) characteristic of native collagen tissue. To generate these higher-order structural features for mimicking a tendon tissue, Fig. 9A shows that we immersed a 200% strain-aligned fibril film in 0.1 M PBS buffer (pH 7.4; 24 hours;

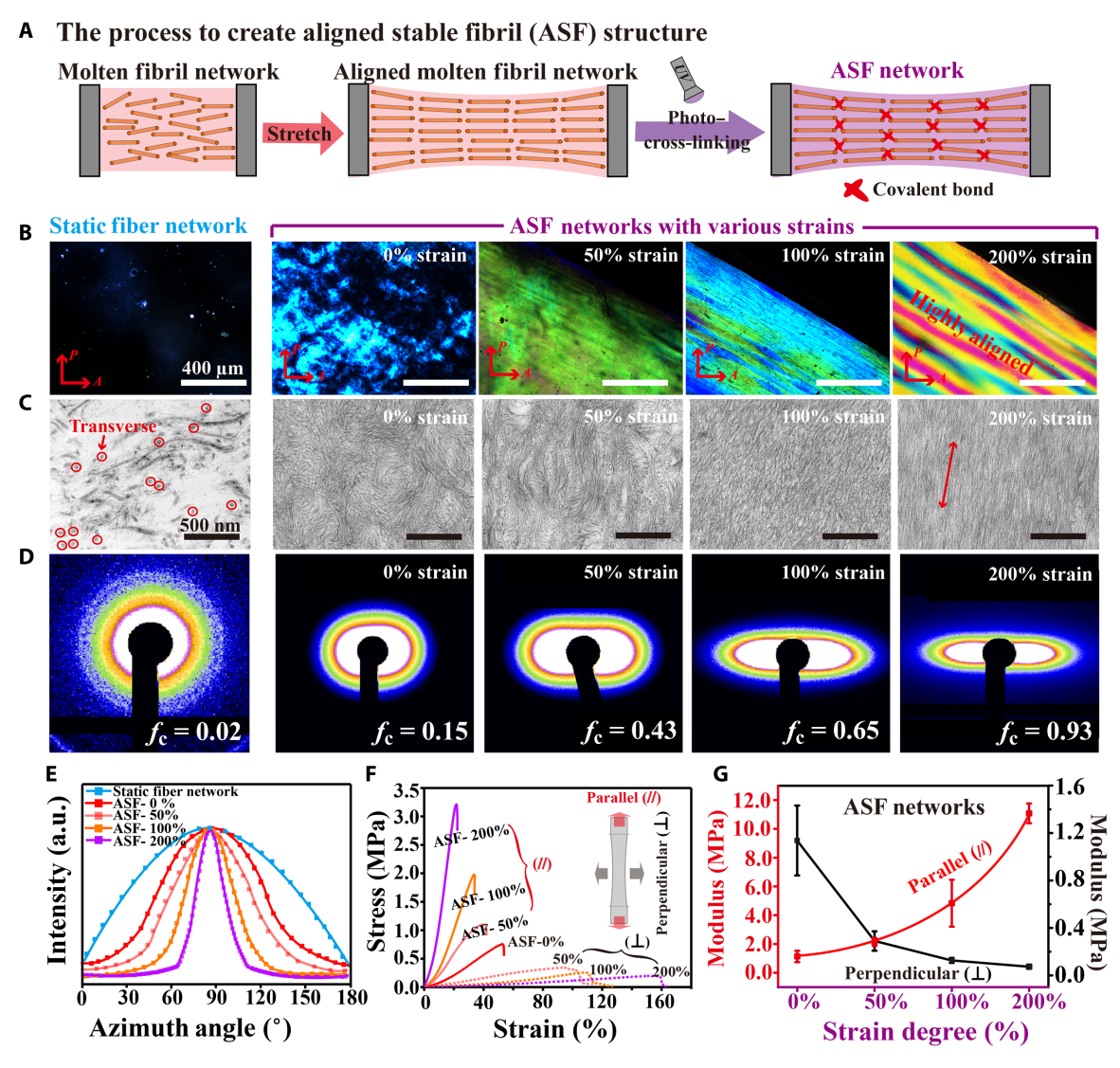


Fig. 8. Aligned stable fibril network processed from molten fibril network. (A) Illustration of the process to fabricate ASF network: The molten fibril network is aligned by mechanical stretching, followed by cross-linking using UV/riboflavin. (B) Polarizing optical microscopy images of cross-linked static fiber network and ASF networks with various strain. The static fiber network has no optical birefringence, indicating an isotropic structure; the ASF network shows a gradually increased optical birefringence in a strain-dependent manner, indicating a strain-induced alignment of the fibrils. (C) TEM images (D) 2D SAXS patterns (f_c is the Herman's orientation parameter) and (E) the azimuthal-integrated intensity distribution curves further indicate the anisotropic aligned nanofibril structure in ASF network. (F) Stress-strain curves of ASF networks in wet state, indicating anisotropic mechanical properties. Tests were performed both parallel and perpendicular to the strain direction. (G) Young's modulus in parallel and perpendicular directions of ASF networks.

room temperature) under a constant external traction to allow a further collagen assembly. The constant external traction is expected to maintain fibril orientation, while incubation in PBS has previously been shown to induce collagen's D-banding and fiber formation through mechanisms that are not entirely understood (37, 58). After incubation, the film was covalently cross-linked by UV/riboflavin treatment. This terminal structure was then characterized at different length scales (Fig. 9B) and compared to the structure of native collagen from rabbit tendon (Fig. 9D). The leftmost micrographs in Fig. 9B show that the generated film has a milky opaque appearance with millimeter scale–striped patterning similar to that of the native tendon collagen. High- and low-magnification SEM images [the middle and rightmost of Fig. 9 (B and D)] further show that both the fabricated film and native collagen are composed of

micrometer-sized, densified, and aligned fibers. Each micrometer-sized fiber was organized of densified aligned of nanoscaled fibrils. The 2D-SAXS pattern shows stretched scattering rings for the fabricated film (Fig. 9C), which are similar to those observed in the native collagen (Fig. 9E) and consistent with the formation of D-bands. Further evidence for D-banding is provided by the 1D SAXS plot in Fig. 9F, which shows numerous scattering peaks that are also similar to those of native tendon collagen. Overall, this structural analysis demonstrates that the partially aligned intermediate molten fibril could be hierarchically organized into densely aligned D-banded fibers with a terminal structure that recapitulates the native microstructure of tendon collagen.

The hierarchically organized structure of native collagen confers mechanical strength to tendon, a functional feature that has been

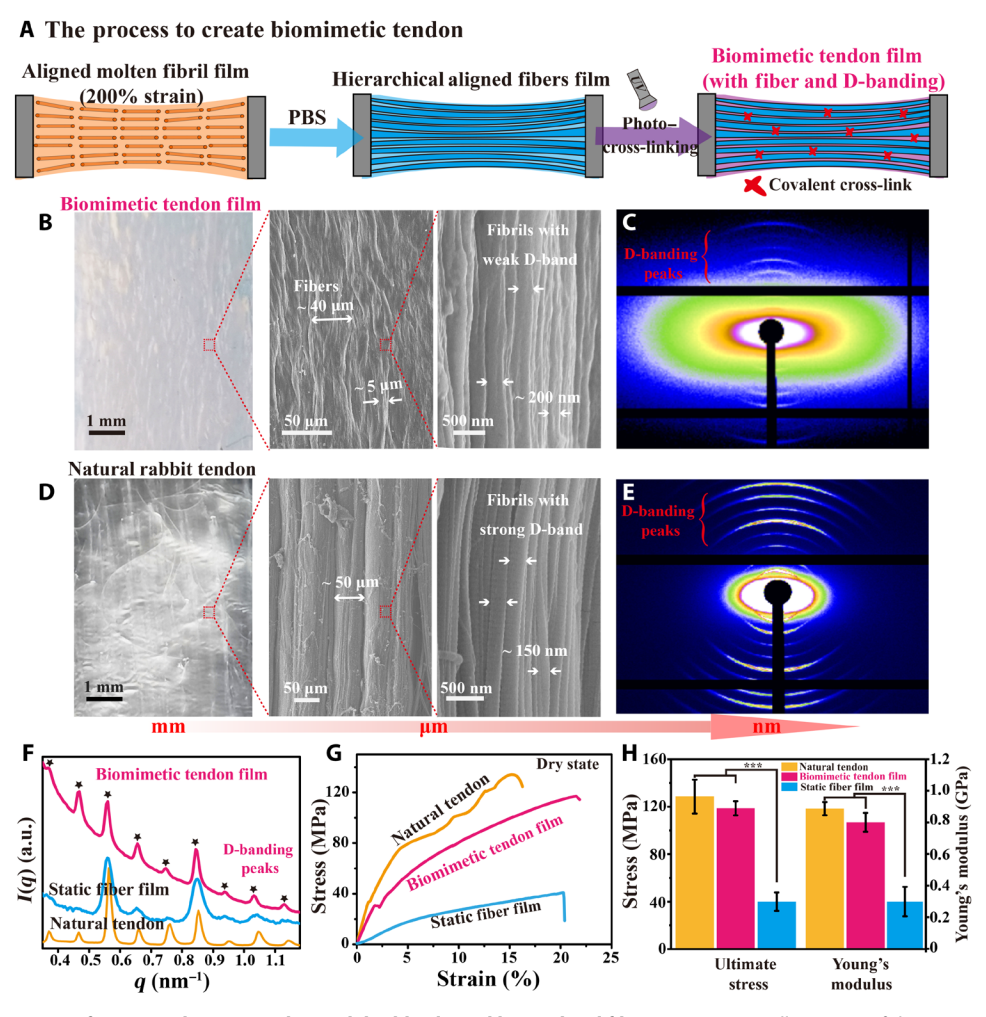


Fig. 9. Biomimetic preparation of a terminal tissue tendon with highly aligned hierarchical fiber structure. (A) Illustration of the process to fabricate biomimetic tendon film: First, the aligned molten fibril network with 200% strain is treated by 0.1 M PBS to allow a highly ordered assembly under a constant external traction, and then UV/riboflavin is used to covalently cross-link this structure to obtain a biomimetic tendon film (with fiber and D-banding characteristics). Microscopic, SEM views and 2D SAXS patterns of (B and C) the biomimetic tendon film and (D and E) natural rabbit tendon suggest a highly similar hierarchical structure. (F) 1D SAXS plots prove the aligned structure and D-banding presented in the biomimetic tendon film. (G) Stress-strain curves and (H) the quantitative ultimate stress and Young's modulus of dried samples indicate that the biomimetic tendon film has similar mechanical properties to the natural tendon tissue (***P < 0.001).

difficult to recapitulate with fabricated collagen matrices. In a final study, we performed stress-strain measurements to compare the mechanical properties of rabbit tendon with those from the biomimetic tendon film and the static fiber film fabricated by a solution assembly method. Because of the differences in water content (i.e., our artificial films have higher water content than the extracted rabbit tendon), we performed all measurements after drying. The stress-strain curves (Fig. 9G) and summarized data (Fig. 9H) show that the biomimetic tendon film can approximate the mechanical properties of native tendon. In summary, these results indicate that the electro-assembled molten fibril network can be processed to form a terminal biomimetic tissue that recapitulates important structural and functional features of native collagen.

DISCUSSION

In summary, we report an electrofabrication method to create an intermediate molten fibril state for collagen. This intermediate state

is composed of partially aligned fibrils with limited higher-order structure that is assembled through reversible interactions. We show that this molten fibril state is adaptive: Its structure and assembly interactions can be adjusted by externally applied physical or chemical cues, and its properties can be dynamically responsive (e.g., self-stiffening, self-contracting, self-healing, and self-shaping). Furthermore, this molten fibril network can be guided to form a higher-ordered terminal structure (i.e., aligned fibers with characteristic D-banding) that recapitulates the structural and functional properties of native collagen-based tissues (e.g., tendons). Overall, this work illustrates the unprecedented capabilities of electrofabrication to provide a controllable set of cues (pH and electric field) that can modulate the macromolecular interactions and alignment responsible for the emergence of dynamic and/or biomimetic structures and functions.

On the basis of these results, we envision future work in three broad areas. First, we envision that this work will motivate further fundamental study of the underlying intermolecular mechanisms that are responsible for the emergence of soft matter structure and that enable dynamic functional properties. Second, we envision that this work furthers the development of electrofabrication as a bottom-up additive manufacturing method (either alone or in combination with other top-down methods such as 3D printing) to enable the hierarchical assembly of soft matter while controlling structure at multiple length scales (nano, micro, and macro). Third, this work advances our technological capabilities for creating collagen-based materials that better mimic native collagen and thus we envision the use of electrofabricated collagen-based materials for important applications in regenerative medicine (e.g., cornea and tendon replacement and bone repair).

MATERIALS AND METHODS

Sample preparation and morphology observation

Acid-extracted collagen I from porcine skin was purchased from Haohai Biological Technology Co. Ltd. (China). Collagen was purified to remove insoluble impurities and dialyzed (Mw cutoff = 7 kDa) to remove soluble salt before use. In all experiments, ultrapure water prepared in a two-stage Milipore Milli-Q Plus purification system was used for solution preparation. The three-electrode system (CHI 660E) used for electro-assembly used Ti plate (2 cm by 3 cm) as a working electrode, Ag/AgCl as a reference electrode, and Pt wire as a counter electrode. Collagen solution (0.5%, w/v; pH 3.5) was prepared by dissolving I type collagen in HAc and then immersed the electrodes into collagen solution described above that was supplemented with 0.1 M H₂O₂ (H₂O₂ is used during collagen electro-assembly to allow a pH gradient to be generated at lower reducing voltages without H₂ gas generation). The following half-reactions resulted in the generation of a pH gradient between the electrodes: anode: $2H_2O - 4e^- \rightarrow 4H^+ + O_2$; cathode: $4H_2O + 4e^ \rightarrow$ 4OH⁻ + 2H₂. The electrodes were applied with a constant current density (8 mA/cm²) for predetermined time of 15 min. The resultant collagen-coated electrode was rinsed extensively with water and ethanol and then peeled the collagen film off from the electrode. For comparison, solution assembly methods reported extensively in the literature were used to fabricate the control samples (27, 35, 36); briefly, collagen solution (0.5%, w/v; pH 3.5) was initially adjusted to a neutral pH 7.2 by 0.5 M NaOH, then casted (collagen content per unit area is the same as the electro-assembled collagen film), and incubated at 37°C for 12 hours for complete gelation.

The surface morphological analysis was performed on SEM (S-4800, Hitachi). The internal ultrastructure observation was performed on TEM (JEM-2100, JEOL). The collagen films were initially dehydrated using a graded series of ethanol and embedded in Eponate12 resin. Thin sections, 60 to 90 nm, were placed on naked copper grids and then stained with uranyl acetate and lead. Images were taken operated at an acceleration voltage of 80 kV. SAXS experiments were performed in the BL19U2 SAXS beamline of the Shanghai Synchrotron Radiation Facility in China. The scattering data were acquired with x-ray beam illumination at a sample-to-detector distance of 1900 mm. The samples were measured for 60 s to obtain scattering signals. 2D SAXS data were averaged into 1D curves of scattering intensity versus q. The backgrounds were set as a polynomial function that passed through the scattering minima of each SAXS curve.

Dynamic adaptability of samples to mechanical forces

The mechanical force's adaptability of collagen samples (strip-shaped hydrogel, 10 mm by 0.5 mm by 30 mm) were first performed using

a Biodynamic chamber with an Electro-Force 3200 testing machine (TA, USA) at room temperature. Under the tensile-fracture model, the tensile rate was set at 10 mm min⁻¹, the strain of samples were estimated as the length change related to the initial length of the sample, and the stress was obtained by dividing the force by the initial cross-sectional area of the hydrogel. Under the dynamic cyclic model, the loading and unloading processes of samples were undergone between a minimum value (0.001 N) and a maximum value (0.04 N for molten fibril samples and 0.16 N for static fiber samples). The change of Young's modulus (MPa, the slope of the initial linear region of the stress-strain curve) and DR (*D*, the calculation formula was shown in the Supplementary Materials) were quantified by the cyclic curve. The stress relaxation was test under a same initial stress at 0.1 MPa or the same initial strain at 20% of then to record the stress change.

Dynamic adaptability of samples to Hofmeister ions and its applications in vivo

Samples were soaked in different species of Hofmeister salts to observe their response. In particular, samples were soaked in gradient concentration of ammonium sulfate solutions at room temperature for 12 hours to strengthen hydrophobic interactions and then performed the tensile test. The Young's modulus (MPa) and toughness (MJ m⁻³, the integral area of tensile stress-strain curve) of samples were calculated by the stress-strain curves (strain rate: 10 mm min⁻¹). For the successive loading-unloading tests, the strain rate was fixed at 100 mm min⁻¹. The total toughness of samples was calculated by the integral area of loading tensile stress-strain curve (MJ m⁻³). And dissipated parts of samples were calculated by total toughness minus the integral area of unloading tensile stressstrain curve (MJ m⁻³); more calculation detail is shown in fig. S8. For applications, 2 M Na₂CO₃-strengthened molten fibril band was further applied in vivo, and all in vivo procedures were approved by the Animal Research Committee. Two-month-old New Zealand white rabbits were used for this experiment, and the rabbit was anesthetized by ear vein injection with 40 to 45 mg kg⁻¹ pentobarbital. Color Doppler ultrasound was first used to observe pulmonary artery and record the diameter and then test the blood flow velocity (VEL) and pressure gradient (PG) of each rabbit before decompression of pulmonary artery surgery. Then, the left ventricular was exposed after opening the chest. First, expose the pulmonary aorta and determine the position of the ring contraction, then the molten fibril hydrogel band was bypassed around the pulmonary aorta and tie a slipping hydrogel knot, then adjust the degree of ring contraction and tighten the gel knot, and lastly, remove the excess gel material. In the end of operation, the rabbit chest was closed according to the routine clinical steps. The diameter of constricted pulmonary artery, VEL, and PG value after operation was tested to confirm the decompression effect. In the following 1 and 3 days, the pulmonary artery diameter recovery was observed by Color Doppler ultrasound; related detection parameters are shown in fig. S13.

Dynamic adaptability of samples to gold anionic clusters and programmable 3D self-shaping

Samples were soaked in chloroauric acid (HAuCl₄; 0.1 M; pH 2; room temperature) for 10 min to investigate the stimuli-contracting kinetics and self-healing. XPS (ESCALAB 250Xi, Thermo Fisher Scientific) and XRD (D/Max2550VB, Japan) was used to detect the existence form of gold ion clusters in samples. Then, the viscoelastic

behavior and stress-strain curve of the samples were measured by a Thermo Haake RS600 rheometer and mechanical tensile machine, respectively. Janus collagen films were further prepared to realize the programmable 3D self-shaping. Molten fibril film and static fiber film were obtained as previous protocol, then the two films were contacted each other under applied external pressure and dried in the air, and they enable to be stably integrated together by hydrogen bonds to form a Janus collagen film. Specific Janus film shapes (i.e., strip shape and flower shape) were used to investigate the stimulated self-shaping kinetics of the Janus films. And any intermediate 3D shape enables to fix by transferred the shaped Janus film to PBS (pH 7.2) and triggers the in situ formation of AuNPs. Patterned process was achieved by soaking the filter paper with different pattern into glutaraldehyde solution (0.1%, w/v) and then putting it on the Janus collagen film surfaces for 30 min, and these patterned films were further prepared to observe the patterned self-shaping. To investigate the biocompatibility of gold collagen composite, L929 fibroblasts were seeded onto the samples (circles with 10 mm in diameter) at 5×10^4 cells per well and culture for cell viability, proliferation tests.

Preparation of aligned stable fibril network and biomimetic tendon structure

Aligned structure of molten fibril networks was produced by applying different strain degrees (50, 100, and 200% with an initial deformation area length of 10 mm) along the length direction, and these further aligned networks were soaking in ethanol to temporarily fix the aligned structure. Then, the aligned fibril networks were immersed in 0.1% (w/v) riboflavin solution [dissolved in 90% (v/v) ethanoll, and UV light (365 nm) induced light cross-linking for 24 hours to obtain the aligned stable fibril networks (i.e., ASF networks and aligned fibrils without D-banding). For the biomimetic tendon fabrication, molten fibril networks were first aligned by applying 200% strain degrees (with an initial deformation area length of 10 mm) of stretching along the length direction, and the further aligned network was soaked in a physiological ionic environment solution [0.1 M PB with sodium chloride (8 mg/ml) for 24 hours] under continuous loading of external forces to induce the D-banding and large diameter aligned fibers formation. Then, UV light cross-linking was performed to fix the biomimetic higher-order hierarchical structure (i.e., aligned fibers with D-banding). Polarizing microscope (POM), TEM, and SAXS were used to the characteristic anisotropic structure of ASF networks and biomimetic tendon and then measured the mechanical properties of these samples.

Statistical analysis

All data were expressed with mean SD and analyzed using one-way analysis of variance with post hoc tests. Significance was set at P < 0.05 (***P < 0.001, **P < 0.01, and *P < 0.05).

SUPPLEMENTARY MATERIALS

Supplementary material for this article is available at https://science.org/doi/10.1126/science.doi/10.1126/

View/request a protocol for this paper from Bio-protocol.

REFERENCES AND NOTES

 P. Tseng, B. Napier, S. W. Zhao, A. N. Mitropoulos, M. B. Applegate, B. Marelli, D. L. Kaplan, F. G. Omenetto, Directed assembly of bio-inspired hierarchical materials with controlled nanofibrillar architectures. *Nat. Nanotechnol.* 12, 474–480 (2017).

- L. Cera, G. M. Gonzalez, Q. Liu, S. Choi, C. O. Chantre, J. Lee, R. Gabardi, M. C. Choi, K. Shin, K. K. Parker, A bioinspired and hierarchically structured shape-memory material. *Nat. Mater.* 20, 242–249 (2021).
- K. Liu, Y. T. Kang, Z. Q. Wang, X. Zhang, 25th anniversary article: Reversible and adaptive functional supramolecular materials: "Noncovalent Interaction" matters. *Adv. Mater.* 25, 5530–5548 (2013).
- A. Walther, Viewpoint: From responsive to adaptive and interactive materials and materials systems: A roadmap. Adv. Mater. 32, 1905111 (2020).
- A. Grinthal, J. Aizenberg, Adaptive all the way down: Building responsive materials from hierarchies of chemomechanical feedback. Chem. Soc. Rev. 42, 7072–7085 (2013).
- R. Merindol, A. Walther, Materials learning from life: Concepts for active, adaptive and autonomous molecular systems. Chem. Soc. Rev. 46, 5588–5619 (2017).
- J. R. Capadona, K. Shanmuganathan, D. J. Tyler, S. J. Rowan, C. Weder, Stimuli-responsive polymer nanocomposites inspired by the sea cucumber dermis. *Science* 319, 1370–1374 (2008).
- L. M. de Espinosa, W. Meesorn, D. Moatsou, C. Weder, Bioinspired polymer systems with stimuli-responsive mechanical properties. Chem. Rev. 117, 12851–12892 (2017).
- T. Motokawa, A. Tsuchi, Dynamic mechanical properties of body-wall dermis in various mechanical states and their implications for the behavior of sea cucumbers. *Biol. Bull.* 205. 261–275 (2003).
- Q. H. Fan, Y. Zheng, X. C. Wang, R. P. Xie, Y. Ding, B. Y. Wang, X. Y. Yu, Y. Lu, L. Y. Liu, Y. L. Li, M. Li, Y. J. Zhao, Y. Jiao, F. F. Ye, Dynamically re-organized collagen fiber bundles transmit mechanical signals and induce strongly correlated cell migration and self-organization. *Angew. Chem. Int. Ed.* 60, 11858–11867 (2021).
- A. C. D. Gonzalez, T. F. Costa, Z. D. Andrade, A. R. A. P. Medrado, Wound healing A literature review. An. Bras. Dermatol. 91, 614–620 (2016).
- P. F. Lu, K. Takai, V. M. Weaver, Z. Werb, Extracellular matrix degradation and remodeling in development and disease. CSH Perspect. Biol. 3, a005058 (2011).
- J. J. Allen, G. R. R. Bell, A. M. Kuzirian, R. T. Hanlon, Cuttlefish skin papilla morphology suggests a muscular hydrostatic function for rapid changeability. *J. Morphol.* 274, 645–656 (2013).
- J. J. Allen, G. R. R. Bell, A. M. Kuzirian, S. S. Velankar, R. T. Hanlon, Comparative morphology of changeable skin papillae in octopus and cuttlefish. J. Morphol. 275, 371–390 (2014).
- J. H. Pikul, S. Li, H. Bai, R. T. Hanlon, I. Cohen, R. F. Shepherd, Stretchable surfaces with programmable 3D texture morphing for synthetic camouflaging skins. Science 358, 210–214 (2017).
- L. Wang, P. C. Uhlig, E. F. Eikenberry, H. Robenek, P. Bruckner, U. Hansen, Lateral growth limitation of corneal fibrils and their lamellar stacking depend on covalent collagen crosslinking by transglutaminase-2 and lysyl oxidases, respectively. J. Biol. Chem. 289, 921–929 (2014).
- P. Kumar, A. Pandit, D. I. Zeugolis, Progress in corneal stromal repair: From tissue grafts and biomaterials to modular supramolecular tissue-like assemblies. *Adv. Mater.* 28, 5381–5399 (2016).
- B. M. Oosterlaken, M. P. Vena, G. de With, In vitro mineralization of collagen. Adv. Mater. 33, 2004418 (2021).
- M. Tzaphlidou, Bone architecture: Collagen structure and calcium/phosphorus maps. J. Biol. Phys. 34, 39–49 (2008).
- M. Franchi, A. Trire, M. Quaranta, E. Orsini, V. Ottani, Collagen structure of tendon relates to function. Sci. World J. 7, 404–420 (2007).
- P. Kannus, Structure of the tendon connective tissue. Scand. J. Med. Sci. Sports 10, 312–320 (2000).
- A. Pissarenko, M. A. Meyers, The materials science of skin: Analysis, characterization, and modeling. *Prog. Mater. Sci.* 110, 100634 (2020).
- A. Sorushanova, L. M. Delgado, Z. N. Wu, N. Shologu, A. Kshirsagar, R. Raghunath,
 A. M. Mullen, Y. Bayon, A. Pandit, M. Raghunath, D. I. Zeugolis, The collagen suprafamily:
 From biosynthesis to advanced biomaterial development. Adv. Mater. 31, e1801651
 (2019)
- 24. Y. Pei, L. Wang, K. Y. Tang, D. L. Kaplan, Biopolymer nanoscale assemblies as building blocks for new materials: A review. *Adv. Funct. Mater.* **31**, 2008552 (2021).
- K. M. Pawelec, S. M. Best, R. E. Cameron, Collagen: A network for regenerative medicine. J. Mater. Chem. B 4, 6484–6496 (2016).
- K. L. Lin, D. W. Zhang, M. H. Macedo, W. G. Cui, B. Sarmento, G. F. Shen, Advanced collagen-based biomaterials for regenerative biomedicine. *Adv. Funct. Mater.* 29, 1804943 (2019).
- S. Majumdar, X. K. Wang, S. D. Sommerfeld, J. J. Chae, E. N. Athanasopoulou, L. S. Shores, X. D. Duan, L. M. Amzel, F. Stellacci, O. Schein, Q. Y. Guo, A. Singh, J. H. Elisseeff, Cyclodextrin modulated type I collagen self-assembly to engineer biomimetic cornea implants. Adv. Funct. Mater. 28, 1804076 (2018).
- M. Younesi, A. Islam, V. Kishore, J. M. Anderson, O. Akkus, Tenogenic induction of human MSCs by anisotropically aligned collagen biotextiles. *Adv. Funct. Mater.* 24, 5762–5770 (2014).

SCIENCE ADVANCES | RESEARCH ARTICLE

- W. Daly, L. Yao, D. Zeugolis, A. Windebank, A. Pandit, A biomaterials approach
 to peripheral nerve regeneration: Bridging the peripheral nerve gap and enhancing
 functional recovery. J. R. Soc. Interface 9, 202–221 (2012).
- I. Sallent, H. Capella-Monsonis, P. Procter, I. Y. Bozo, R. V. Deev, D. Zubov, R. Vasyliev, G. Perale, G. Pertici, J. Baker, P. Gingras, Y. Bayon, D. I. Zeugolis, The few who made it: Commercially and clinically successful innovative bone grafts. Front. Bioeng. Biotechnol. 8, 952 (2020).
- Y. Pei, K. E. Jordan, N. Xiang, R. N. Parker, X. Mu, L. Zhang, Z. B. Feng, Y. Chen, C. M. Li, C. C. Guo, K. Y. Tang, D. L. Kaplan, Liquid-exfoliated mesostructured collagen from the bovine achilles tendon as building blocks of collagen membranes. ACS Appl. Mater. Interfaces 13, 3186–3198 (2021).
- X. Wang, O. Yue, X. Liu, M. Hou, M. Zheng, A novel bio-inspired multi-functional collagen aggregate based flexible sensor with multi-layer and internal 3D network structure. Chem. Eng. J. 392, 123672 (2020).
- L. M. Delgado, N. Shologu, K. Fuller, D. I. Zeugolis, Acetic acid and pepsin result in high yield, high purity and low macrophage response collagen for biomedical applications. *Biomed. Mater.* 12, 065009 (2017).
- L. Salvatore, N. Gallo, M. L. Natali, A. Terzi, A. Sannino, M. Madaghiele, Mimicking the hierarchical organization of natural collagen: Toward the development of ideal scaffolding material for tissue regeneration. Front. Bioeng. Biotechnol. 9, 644595 (2021).
- L. M. Delgado, K. Fuller, D. I. Zeugolis, Collagen cross-linking: Biophysical, biochemical, and biological response analysis. *Tissue Eng. Pt. A* 23, 1064–1077 (2017).
- S. T. Kreger, B. J. Bell, J. Bailey, E. Stites, J. Kuske, B. Waisner, S. L. Voytik-Harbin, Polymerization and matrix physical properties as important design considerations for soluble collagen formulations. *Biopolymers* 93, 690–707 (2010).
- X. G. Cheng, U. A. Gurkan, C. J. Dehen, M. P. Tate, H. W. Hillhouse, G. J. Simpson, O. Akkus, An electrochemical fabrication process for the assembly of anisotropically oriented collagen bundles. *Biomaterials* 29, 3278–3288 (2008).
- Y. J. Zhang, S. Furyk, D. E. Bergbreiter, P. S. Cremer, Specific ion effects on the water solubility of macromolecules: PNIPAM and the Hofmeister series. J. Am. Chem. Soc. 127, 14505–14510 (2005).
- K. D. Collins, M. W. Washabaugh, The Hofmeister effect and the behaviour of water at interfaces. Q. Rev. Biophys. 18, 323–422 (1985).
- X. Chen, T. Yang, S. Kataoka, P. S. Cremer, Specific ion effects on interfacial water structure near macromolecules. J. Am. Chem. Soc. 129, 12272–12279 (2007).
- Q. Y. He, Y. Huang, S. Y. Wang, Hofmeister effect-assisted one step fabrication of ductile and strong gelatin hydrogels. Adv. Funct. Mater. 28, 1705069 (2018).
- J. Y. Lin, Y. Huang, S. Y. Wang, The Hofmeister effect on protein hydrogels with stranded and particulate microstructures. *Colloids Surf. B* 196. 111332 (2020).
- L. R. Khoury, M. Slawinski, D. R. Collison, I. Popa, Cation-induced shape programming and morphing in protein-based hydrogels. Sci. Adv. 6, eaba6112 (2020).
- 44. L. R. Khoury, I. Popa, Chemical unfolding of protein domains induces shape change in programmed protein hydrogels. *Nat. Commun.* **10**, 5439 (2019).
- M. A. Gonzalez, J. R. Simon, A. Ghoorchian, Z. Scholl, S. T. Lin, M. Rubinstein, P. Marszalek, A. Chilkoti, G. P. Lopez, X. H. Zhao, Strong, tough, stretchable, and self-adhesive hydrogels from intrinsically unstructure proteins. *Adv. Mater.* 29, 1604743 (2017).
- M. K. Sing, W. R. Burghardt, B. D. Olsen, Influence of end-block dynamics on deformation behavior of thermoresponsive elastin-like polypeptide hydrogels. *Macromolecules* 51, 2951–2960 (2018).
- W. X. Sun, B. Xue, Q. Y. Fan, R. H. Tao, C. X. Wang, X. Wang, Y. R. Li, M. Qin, W. Wang, B. Chen, Y. Cao, Molecular engineering of metal coordination interactions for strong, tough, and fast-recovery hydrogels. *Sci. Adv.* 6, eaaz9531 (2020).
- W. W. Huang, A. Tarakanova, N. Dinjaski, Q. Wang, X. X. Xia, Y. Chen, J. Y. Wong, M. J. Buehler, D. L. Kaplan, Design of multistimuli responsive hydrogels using integrated modeling and genetically engineered silk-elastin-like proteins. *Adv. Funct. Mater.* 26, 4113–4123 (2016).

- A. Bauer, M. Khalii, D. Schmidt, S. Recla, J. Bauer, A. Esmaeili, G. Penford, H. Akintuerk, D. Schranz, Transcatheter left atrial decompression in patients with dilated cardiomyopathy: Bridging to cardiac transplantation or recovery. *Cardiol. Young* 29, 355–362 (2019).
- G. M. Barker, J. M. Forbess, K. J. Guleserian, A. W. Nugent, Optimization of preoperative status in hypoplastic left heart syndrome with intact atrial septum by left atrial decompression and bilateral pulmonary artery bands. *Pediatr. Cardiol.* 35, 479–484 (2014).
- S. D. Miyamoto, B. A. Pietra, K. C. Chan, D. D. Ivy, C. Mashburn, D. N. Campbell, M. B. Mitchell, M. M. Boucek, Long-term outcome of palliation with internal pulmonary artery bands after primary heart transplantation for hypoplastic left heart syndrome. *Pediatr. Cardiol.* 30, 419–425 (2009).
- S. C. Huang, X. X. Xia, R. X. Fan, Z. G. Qan, Programmable electrostatic interactions expand the landscape of dynamic functional hydrogels. *Chem. Mater.* 32, 1937–1945 (2020).
- Y. X. Deng, Q. Zhang, B. L. Feringa, H. Tian, D. H. Qu, Toughening a self-healable supramolecular polymer by ionic cluster-enhanced iron-carboxylate complexes. *Angew. Chem. Int. Edit.* 59, 5278–5283 (2020).
- R. T. Xing, K. Liu, T. F. Jiao, N. Zhang, K. Ma, R. Y. Zhang, Q. L. Zou, G. H. Ma, X. H. Yan, An injectable self-assembling collagen-gold hybrid hydrogel for combinatorial antitumor photothermal/photodynamic therapy. *Adv. Mater.* 28, 3669–3676 (2016).
- D. Cabuzu, A. Cirja, R. Puiu, A. M. Grumezescu, Biomedical applications of gold nanoparticles. Curr. Top. Med. Chem. 15, 1605–1613 (2015).
- P. M. Tiwari, K. Vig, V. A. Dennis, S. R. Singh, Functionalized gold nanoparticles and their biomedical applications. *Nanomaterials* 1, 31–63 (2011).
- R. R. Xing, T. F. Jiao, L. Y. Yan, G. H. Ma, L. Liu, L. R. Dai, J. B. Li, H. Mohwald, X. H. Yan, Colloidal gold-collagen protein core-shell nanoconjugate: One-step biomimetic synthesis, layer-by-layer assembled film, and controlled cell growth. ACS Appl. Mater. Interfaces 7, 24733–24740 (2015).
- B. R. Williams, R. A. Gelman, D. C. Poppke, K. A. Piez, Collagen fibril formation. Optimal in vitro conditions and preliminary kinetic results. J. Biol. Chem. 253, 6578–6585 (1978).

Acknowledgments: We appreciate X. Miu (BL19U2 beamline of Shanghai Synchrotron Radiation Facility) for help in synchrotron SAXS test, and we thank the Research Center of Analysis and Test of East China University of Science and Technology for help on the material characterization and we also appreciate the Shanghai Frontiers Science Center of Optogenetic Techniques for Cell Metabolism for their valuable advices to this work. **Funding:** This research was supported by the National Natural Science Foundation of China (31922041, 51621002, and 11932012), the Science and Technology Innovation Project and Excellent Academic Leader Project of Shanghai Science and Technology Committee (21S31901500, 21XD1421100), the Fundamental Research Funds for the Central Universities (JKVD1211032 and JKVD1211002), and U.S. National Science Foundation (CBET-1932963). Author contributions: M.L. conceived the ideas for experimental designs, executed the majority of the experiments. analyzed data, and wrote the original manuscript. H.W. supported the fabrication of the materials and the characterization of mechanical properties of materials. X.Q., D.J., and M.Y. participated in animal experimental design. D.J. and H.W. assisted with animal surgery. S.W. and Z.Z participated in the discussion of the project and data analysis. G.F.P. proposed the concept of intermediate molten fibril state and participated the writing and revision of original manuscript. X.Q. reviewed and edited the original manuscript and finalized the manuscript. X.Q. and C.L. supervised the project and provided financial support. Competing interests: The authors declare that they have no competing interests. Data and materials availability: All data needed to evaluate the conclusions in the paper are present in the paper and/or the Supplementary Materials.

Submitted 3 August 2021 Accepted 8 December 2021 Published 2 February 2022 10.1126/sciadv.abl7506

Downloaded from https://www.science.org on February 07, 2022

Science Advances

Electro-assembly of a dynamically adaptive molten fibril state for collagen

Miao LeiXue QuHaoran WanDawei JinShijia WangZhiling ZhaoMeng YinGregory F. PayneChangsheng Liu

Sci. Adv., 8 (5), eabl7506. • DOI: 10.1126/sciadv.abl7506

View the article online

https://www.science.org/doi/10.1126/sciadv.abl7506

Permissions

https://www.science.org/help/reprints-and-permissions